

Inverse heat problem of determining unknown surface heat flux in a molten salt loop

M. Fernández-Torrijos^{a,*}, C. Sobrino^a, J. A. Almendros-Ibáñez^{b,c}, C. Marugán-Cruz^a, D. Santana^a

^a*Universidad Carlos III de Madrid, ISE Research Group, Thermal and Fluid Engineering Department, Avda. de la Universidad 30, 28911 Leganés, Madrid, Spain*

^b*E.T.S. de Ingenieros Industriales de Albacete, Dpto. de Mecánica Aplicada e Ingeniería de Proyectos, Castilla La Mancha University, Campus universitario s/n, 02071, Albacete, Spain*

^c*Renewable Energy Research Institute, Section of Solar and Energy Efficiency, C/ de la Investigación s/n, 02071, Albacete, Spain*

Abstract

Inverse heat transfer problems typically rely on temperature measurements for estimating unknown boundary heat flux, such as that in the water tubes of steam boilers or central receivers in solar tower power plants. In this work, an experimental facility consisting of a molten salt loop that simulates a tube of a solar tower receiver is presented to obtain the outer tube surface temperatures under solar tower power plant operating conditions. The external surface of the pipe in the test section is heated in a controlled manner with an induction heater, which provides a very high nonuniform heat flux. An inverse thermal method has been applied to obtain the incident heat flux onto the receiver tube from the outer surface temperature measurements. To solve the inverse problem, a transient two-dimensional numerical model of a circular pipe flowing molten nitrate salt and subjected to a nonhomogeneous circumferential heat flux has been developed. The heat flux calculation with the inverse method is in accordance with the heat flux estimation based on the calibration of the induction heater. A good agreement between the experimental and calculated temperatures is observed. Furthermore, the deflection of the tube caused by

*Corresponding author. Tel.: +34 916246224

Email address: ftorrijo@ing.uc3m.es (M. Fernández-Torrijos)

the nonhomogeneous heat flux is measured and is compared to the deflection calculated from the radial temperature profile from the inverse problem solution, and a good agreement between both results is observed.

Keywords: Inverse heat conduction problem, Inductor coil, Central receiver, Tube bending.

1. Introduction

Concentrating Solar Power (CSP) with Thermal Energy Storage (TES) is a key technology to contribute to increasing the penetration of renewable energy in the electricity mix and to the reduction of greenhouse gas emissions, since it increases the flexibility of the electricity system avoiding the need of fossil fuel back up. A typical CSP plant consist of: i) a solar concentrator, where the solar radiation is reflected; ii) the receiver, where the solar radiation is transferred to the heat transfer fluid (HTF); iii) the TES system, where the thermal energy is stored; iv) the heat exchangers, where the heat is transferred from the HTF of the storage system to the working fluid of the power block and v) the power block, that converts the thermal energy into electricity. The main CSP systems are linear Fresnel reflectors, central receivers (power towers), parabolic trough and parabolic dish systems. A linear Fresnel consists of a large number of mirrors in parallel rows plane or slightly curved that reflect the sunlight to a pipe above. Power tower or central receiver systems utilize sun-tracking mirrors called heliostats to focus sunlight onto a receiver at the top of a tower. In a parabolic trough CSP system, radiation is concentrated by parabolically curved, trough-shaped reflectors onto a receiver pipe running along about a meter above the curved surface of the mirrors. A Parabolic dish system consists of a parabolic-shaped point focus concentrator in the form of a dish that reflects solar radiation onto a receiver mounted at the focal point. Today's most advanced CSP systems are central receivers integrated with 2-tank TES, working with nitrate molten salt both in the receiver and in the storage system and delivering thermal energy at 565°C for integration with conventional steam-Rankine

25 power cycles. Receiver tubes can reach very high temperatures of 650-750°C
26 and are exposed to a nonuniform solar flux that can exceed 1.0 MW/m². This
27 results in an uneven temperature distribution in the circumferential direction,
28 resulting in thermal stresses (Marugán-Cruz et al., 2016) and deflections in the
29 receiver tubes that can reduce their service life. In central external receivers,
30 the flux distribution is designed to heat the salt from 290°C to 565°C while
31 keeping the strain and corrosion in the receiver tubes within allowable limits.
32 The receiver temperatures are used as inputs to some of the flux management
33 systems of a commercial plant to make it operate within these limits. Thermo-
34 couples are installed on the back (non-illuminated) wall of the receiver tubes
35 (Pacheco, 2002). The back-wall thermocouples provide information on changes
36 much more quickly than the outlet salt thermocouple because they measure
37 receiver panel information, not just the outlet conditions (Smith and Chavez,
38 1992). Moreover, since the tube wall is relatively small and the thermocouple is
39 placed on the back of the tube (away from the incident flux), the temperature
40 measurement should represent the bulk salt temperature within the tube at that
41 point (Smith and Chavez, 1992).

42

43 The phenomena that occur in different subsystems of a molten salt CSP plant
44 are reproduced in lab-scale molten salt loops to study them under controlled
45 conditions. Some experimental works measured the convection coefficient for
46 the internal flow of molten salt in a pipe at a high Reynolds number that is
47 characteristic of real receivers ($>10^4$). Typically, an electrical heater heats the
48 pipe in the test section, providing uniform heat fluxes in the range of 200-400
49 kW/m² (Yang et al., 2012; Jianfeng et al., 2013a,b; Kim et al., 2018). Uniform
50 heat transfer can also be achieved through a heat exchanger with another fluid
51 (Yu-ting et al., 2009; Du et al., 2017). In very few experimental facilities, the
52 heat flux is applied unilaterally to the testing tube. For instance, Xiangyang
53 et al. (2014) measured the Nusselt number of a molten salt in a pipe with a
54 nonuniform heat flux that was considerably higher on one of its sides. They
55 found that the Nusselt number of the side with the highest heat flux was lower

56 than that of the side with the lowest heat flux.

57

58 To produce a higher heat flux similar to that of central receivers, the pipe
59 can be heated in a small area using an inductor. The inductor includes a copper
60 coil and a magnetizer, also called an electromagnetic flux concentrator. As high-
61 frequency alternating current flows in the coil, a high eddy current is induced
62 in the surface layer of the metal piece, which leads to a rapid increase in the
63 temperature of the surface layer (Zhu et al., 2018). When the concentrator is
64 properly designed, a high heating rate and uniform temperatures of the metal
65 piece can be achieved (Gao et al., 2016). When using this heating method, a
66 high wall temperature of the tube is reached. Kruizenga et al. (2014) employed
67 an inductor to uniformly heat the external surface of a 1 m long test section
68 pipe in a pumped-salt test loop where molten nitrate salt circulated to simulate
69 a solar receiver. In particular, the internal surface of the pipe was maintained
70 at a temperature of approximately 670°C to study the decomposition of the
71 salt. However, the determination of this temperature is problematic because
72 it cannot be directly measured and the power applied by the inductor heater
73 cannot be directly taken as the thermal power input of the pipe due to the losses.

74

75 The determination of the heat flux and subsequently the internal surface
76 temperature of the receiver pipe from the measurement of the external surface
77 temperature, which can be accomplished in practice, is of crucial interest in
78 both commercial plants and lab-scale installations. The direct measurements
79 of heat flux on commercial plants is very difficult for a cylindrical receiver, and
80 computer simulations are used instead (Pacheco, 2002).

81

82 Inverse heat conduction problems have generally been associated with the
83 estimation of an unknown boundary heat flux by using temperature measure-
84 ments (Özisik and Orlande, 2000). This is the opposite of a classical direct heat
85 conduction problem where the boundary heat flux is given while the temper-
86 ature field is determined. Several techniques for solving the inverse problem

87 have been developed, for example, the conjugate gradient method, the method
88 of fundamental solutions, linear least-squares methods, analytical methods and
89 genetic algorithms (Alifanov, 1994; Taler and Duda, 2006). In particular, an
90 inverse heat transfer analysis has previously been applied (Yang et al., 2013) to
91 estimate the unknown time-dependent inner-wall heat flux of a hollow cylinder
92 from the knowledge of the temperatures within the medium at different ra-
93 dial positions. The temperature data were simulated to represent temperature
94 measurements with the objective of evaluating the conjugate gradient method
95 proposed to solve the inverse heat transfer problem. Su and Silva-Neto (2001)
96 applied the conjugate gradient method to solve the radial and circumferential
97 transient dependence of source strength in cylindrical rods. Lu et al. (2010)
98 applied an inverse heat conduction problem to obtain the unknown transient
99 fluid temperatures near the inner wall of a pipe elbow with thermal stratifi-
100 cation from simulated outer surface temperature measurements. Besides these
101 numerical solution techniques, analytical methods have been applied to solve
102 inverse heat conduction problems. For instance, Cattani et al. (2015) applied
103 the Quadrupole Method coupled to the Truncated Singular Value Decomposi-
104 tion Approach to estimate the local convective heat transfer coefficient on the
105 internal wall surface of a pipe. Additionally, Maillet et al. (1991) applied the
106 least-squares method coupled to the analytical solution of the 2-D temperature
107 field to the measurement of a heat transfer coefficient on a cylinder. Inverse heat
108 transfer methods have been successfully applied to different technological fields.
109 Taler et al. (2009) developed a heat tubular-type instrument (flux-tube) to mea-
110 sure the heat flux to water walls of combustion chambers based on the inverse
111 heat conduction problem. Thus, they calculated the heat flux absorbed by the
112 walls from surface temperature measurements (Taler et al., 2014). The temper-
113 ature history measured in two-phase boiling experiments during and following
114 the critical heat flux were used in the solution of the two-dimension inverse heat
115 transfer problem to estimate the wall temperatures and wall heat fluxes in water-
116 cooled reactors (Duarte et al., 2018). Perakis and Haidn (2019) applied a 3D
117 inverse method for estimating the time- and spatially resolved heat flux distri-

118 bution at the hot gas wall of rocket combustors. Yadav et al. (2018) developed a
119 two-thermocouple model especially suitable to be applied to time-varying high
120 heat flux applications such as nuclear reactor containments, reactor pressure
121 vessels, furnaces, and jet heating/cooling etc. Liu et al. (2018) obtained an ana-
122 lytical inverse heat transfer solution which can be used to calculate surface heat
123 flux in temperature-sensitive coating measurements in high-enthalpy hypersonic
124 wind tunnels. An inverse heat transfer was also applied to the diagnosis of the
125 lateral refractory brick wall of a melting furnace (Hafid and Lacroix, 2017), al-
126 lowing to predict the time-varying thickness of the protective bank that covers
127 the inner lining of the furnace wall, the thermal contact resistance between the
128 inner lining and the protective bank and the possible erosion of the refractory
129 brick wall. Concerning the solar technology field, inverse heat transfer methods
130 have been applied to predict the heat flux distribution on a flat plate receiver
131 in a solar Concentrating Photovoltaic system using non-intrusive temperature
132 measurement obtained with an IR camera (Reddy et al., 2018).

133

134 In the present paper, an inverse heat transfer method is applied to calculate
135 the heat flux at the outer surface of a pipe conducting molten nitrate salt from
136 outer surface temperature measurements. The measurements were performed
137 in a molten salt loop that simulates the receiver of a solar tower. The external
138 surface of the pipe in the measurement area is heated using an inductor, which
139 provides a very high nonuniform heat flux. Once the heat flux is calculated from
140 the outer surface temperature measurements, the radial temperature profile in
141 the pipe wall is obtained. Additionally, the deflection of the tube caused by the
142 unilateral heat flux is measured, and it is compared to the deflection calculated
143 from the radial temperature profile. Experimental measurements of the outer
144 surface temperature of a receiver tube under solar tower power plant operating
145 conditions have not been reported in the literature before, which can be useful
146 for the validation of tubular external molten salt receiver numerical models.
147 Moreover, for the first time, an inverse heat transfer method has been applied
148 to obtain the incident heat flux onto a solar receiver, which is of interest in both

149 commercial plants and lab-scale installations.

150 **2. Experimental setup**

151 The experiments were performed in a molten salt (60% NaNO_3 /40% KNO_3)
152 test loop (Figure 1) that consists of a cylindrical molten salt tank, a pump, a
153 pressure sensor, the test section and a flow meter. The total length of the loop
154 is greater than 12 m. The 600 l tank is made of AISI316 and is heated by an
155 electrical furnace. The temperature of the molten salt in the tank is controlled
156 to maintain it between 300 °C and 500 °C. A high-temperature pump coupled
157 to an electric motor equipped with a variable-frequency drive allows varying the
158 flow rate through the molten salt loop. The tank is connected to a 304 stainless
159 steel pipe, with a 5.2 cm inner diameter and 4 mm thickness, through which the
160 molten salt circulates, reaching Reynolds numbers in the range of $4 \cdot 10^4$ - $2 \cdot 10^5$.
161 An ultrasonic flow meter allows measuring the flow rate at the test section. The
162 pipe is wrapped with electrical heaters and insulated in the whole loop except in
163 the 0.5 m test section, where an induction heat generator provides a high heat
164 flux that is applied to a small rectangular region of the tube surface such that the
165 inductor reproduces the nonuniform heating conditions of the receiver in a cen-
166 tral tower plant. The induction heater has an output power of 6 kW and output
167 frequency range of 270-450 kHz. The inductor coil is provided with a magnetic
168 flux concentrator that, when properly designed, produces a high heating rate
169 and uniform temperature of the metal piece. To ensure a satisfactory heating
170 process (Gao et al., 2016), the distance between the coil and the heating surface
171 was fixed to 7 mm, the working frequency of the inductor was 300 kHz, and a
172 rectangular coil of 100 mm x 7 mm with a magnetic flux concentrator of 4 mm
173 in width, 4 mm in height, and 100 mm in length was used, as shown in Figure 2.

174

175 The total electric power provided by the induction heater was 4 kW_e in the
176 experiments conducted in the molten salt loop. The heat flux reaching the tube
177 was applied in a rectangular area of 100 mm x 15 mm, which corresponds to

178 the area occupied by the coil and the magnetic flux concentrator. Thus, the
179 maximum heat flux that could reach the external wall of the pipe would be
180 2.67 MW/m^2 . Since the induction coil needs to be chilled with water, part of
181 the heat flux generated by the induction heater is transferred to the stream of
182 water flowing through the coil. Therefore, it is difficult to accurately determine
183 the heat flux that reaches the external wall of the pipe knowing the total elec-
184 tric power of the induction heater. In this work, some experiments to calibrate
185 the induction heater for different electric powers (i.e., 3, 5 and 7 kW_e) were
186 conducted to determine the percentage of the electrical power of the induction
187 heater that is effectively transferred to the tube. With this aim, a 1.5 m long
188 tube made of the same material and with the same inner and outer diameters
189 as those of the tube used in the molten salt loop was heated by the induction
190 coil. The tube was placed vertically, and it was closed at the bottom end and
191 externally insulated using a mineral wool. Then, it was filled with water, and
192 thermocouples were installed to measure the temperature of the water inside the
193 tube and the temperature of the outer surface of the tube wall. Additionally,
194 the flow rate and the inlet and outlet temperatures of the cooling water flowing
195 through the induction coil were measured. According to these measurements,
196 we concluded that approximately 35% of the inductor electrical power is trans-
197 ferred to the inductor cooling water and that only 40% is converted to thermal
198 energy that reaches the tube and heats the wall and the water contained in it.
199 Hence, this calibration experiment indicates that given this 40% efficiency, for
200 the experimental conditions presented in this paper (inductor electrical power
201 of 4 kW_e applied to a $15 \times 100 \text{ mm}$ area), the heat flux applied to the external
202 surface of the tube is approximately 1 MW/m^2 . However, to more accurately
203 predict the heat flux incident on the test section, an inverse algorithm based on
204 the outer surface temperature measurements has been proposed in this work.

205 [Figure 1 about here.]

206 [Figure 2 about here.]

207 To measure the temperature of the external surface of the pipe along the an-

208 gular position, skin thermocouples were used. They consist of a sheath K-type
209 thermocouples embedded in a steel plate to facilitate the welding of the ther-
210 mocouple to the pipe (see Figure 4). A total of 7 thermocouples were used:
211 5 thermocouples welded to the outer surface of the pipe in different positions
212 along the circumferential direction at the axial position corresponding to the
213 center of the coil, and 2 thermocouples inside the pipe at $r = 0$ to measure the
214 bulk salt temperature, located at $z = -0.21$ m and $z = 0.21$ m as shown in
215 Figure 3. In addition, the installation has four sheath K-type thermocouples
216 inside the tank to control the temperature of the salt between 300 °C and 500
217 °C and a thermocouple welded to the tank wall to prevent the temperature
218 from exceeding 550 °C. For data acquisition, National Instruments' 9219 uni-
219 versal analog input acquisition cards were used. This module has 4 channels
220 and has the advantage of having interchannel isolation such that each channel
221 is isolated from all other channels and other noninsulated components to reject
222 interchannel noise and electromagnetic noise from the induction heater.

223

224 Moreover, thermal images were taken with an IR camera (Optris PI640 with
225 O15 telephoto lens) during the experiments to study the deformation of the
226 tube due to the nonuniform heat flux, which results in an uneven temperature
227 distribution, as shown in the left picture of Figure 4. The right picture of Figure
228 4 shows the position of the pipe with uniform tube temperature when the molten
229 salt is flowing through the pipe and the induction coil is not heating the tube.
230 Comparing both pictures and considering that the green rectangle corresponds
231 to the distance between the induction coil and the pipe, the tube bending due to
232 the nonuniform heat flux provided by the induction heater is appreciated. The
233 analysis of the IR camera images over time provided the displacement of the
234 tube with an error of ± 0.2 mm because the size at a single pixel at the object
235 level was 0.4 mm.

236

[Figure 3 about here.]

237

[Figure 4 about here.]

238 **3. Numerical modeling**

239 *3.1. Direct problem*

240 *3.1.1. Heat conduction in pipe wall*

241 In this work, a transient numerical model has been developed to compare
242 the experimental measurements with the numerical results. The heat transfer
243 problem of a circular pipe subjected to a nonhomogeneous heat flux in the
244 circumferential direction while a molten-salt stream is flowing through the pipe
245 is considered. For simplicity, the heat transfer problem along the molten-salt
246 flow is not calculated, and the heat exchange between the molten-salt stream
247 and the pipe wall is solved using Petukhov’s correlation. The physical properties
248 of the salt, which are known functions of temperature (Zavoico, 2001), were
249 calculated at the molten-salt inlet temperature. To solve the heat transfer
250 problem along the pipe wall, a homogeneous heat flux in the axial direction was
251 considered to develop a two-dimensional model of the pipe. Thermal conduction
252 in axial direction was neglected, as negligible temperature difference was shown
253 between one thermocouple placed at the axial position of the center of the coil
254 and another thermocouple at $z = 27$ mm, being both of them at the same
255 angular position. Therefore, the cross section studied in this work, which was
256 placed at the center of the coil, was not affected by the conductive axial heat
257 losses that occurs at the two ends of the heated part, as the temperature field
258 along the length of the induction heater was shown to be uniform. During the
259 postprocessing of the results, it was verified that the heat flux in axial direction
260 computed from the temperature measurements was three order of magnitude
261 lower compared to the total heat flux in radial and circumferential directions, for
262 a cross section placed at the center of the coil. Therefore, heat is transferred by
263 conduction in the radial and circumferential directions along the pipe according
264 to the heat diffusion equation.

$$\rho c_p \frac{\partial T(r, \theta, t)}{\partial t} = \frac{k}{r} \frac{\partial}{\partial r} \left(r \frac{\partial T(r, \theta, t)}{\partial r} \right) + \frac{k}{r^2} \frac{\partial^2 T(r, \theta, t)}{\partial \theta^2} \quad (1)$$

265 where T is the wall temperature, ρ is the wall density, c_p is the wall specific heat,
266 and k is the wall conductivity. The inner wall of the pipe is in contact with the

267 molten salt, so its thermal boundary condition is set to a convective heat transfer
 268 condition. The outer wall of the pipe is in contact with the atmosphere, so its
 269 thermal boundary condition is set to a mixed convective and radiative heat
 270 transfer condition. The initial temperature of the pipe is uniform along the
 271 circumferential direction and, for simplicity, it was considered to be uniform in
 272 radial direction, as the temperature difference between inner and outer surfaces
 273 was approximately 1°C due to the radiative and convective losses to the ambient.
 274 Therefore, the initial temperature was assumed to be the measured temperature
 275 at $r = r_o$ at the beginning of the experiment. Hence, the boundary and initial
 276 conditions of the problem are expressed as follows:

$$-k \frac{\partial T(r, \theta, t)}{\partial r} = h_i (T_s - T(r, \theta, t)) \text{ at } r = r_i \quad (2)$$

$$-k \frac{\partial T(r, \theta, t)}{\partial r} = h_{conv+rad}(\theta, t) (T(r, \theta, t) - T_\infty) - q_{ind}(\theta, t) \text{ at } r = r_o \quad (3)$$

$$\frac{\partial T(r, \theta, t)}{\partial \theta} = 0 \text{ at } \theta = 0, \pi \quad (4)$$

$$T(r, \theta, t) = T_{ini} \text{ for } t = 0 \quad (5)$$

277 where r_i and r_o are the inner and outer pipe radii, respectively; T_s and T_∞ are
 278 the temperatures of the molten salt and surroundings, respectively; h_i is the
 279 convective heat transfer from the molten salt to the inner surface of the wall;
 280 and $h_{conv+rad}$ is the mixed convective and radiative heat transfer from the outer
 281 surface of the pipe to the atmosphere. θ is the circumferential coordinate, which
 282 has its origin at the front part of the pipe, facing the induction coil, as shown
 283 in Figure 5, and q_{ind} is the heat flux from the induction heater applied to the
 284 external wall of the pipe, where q_{ind} was considered to be positive when the
 285 heat flux is coming from the induction heater to the pipe (see Figure 5). Notice
 286 that only half of the tube was simulated due to symmetry. For the experiments
 287 developed in this work, q_{ind} was assumed to be uniform in the area of the pipe
 288 facing the induction coil and the magnetic flux concentrator ($-15^\circ \leq \theta \leq 15^\circ$),
 289 while the area not facing the coil did not receive heat flux from the induction

290 heater (see Figure 5).

$$q_{ind}(\theta, t) = \begin{cases} q_{ind}(t) & \text{if } \theta \leq 15^\circ \\ 0 & \text{if } \theta > 15^\circ \end{cases} \quad (6)$$

291 The convection coefficient h_i was calculated using the correlation proposed by
 292 Petukhov (1970) for turbulent flow, while $h_{conv+rad}$ was obtained as follows:

$$h_{conv+rad}(\theta, t) = h_\infty + \varepsilon \sigma_r (T(r, \theta, t) + T_\infty) (T^2(r, \theta, t) + T_\infty^2) \quad (7)$$

293 where h_∞ is the convection coefficient from the outer surface of the pipe to the
 294 atmosphere, σ_r is the Stefan-Boltzmann constant, and ε is the AISI304 sur-
 295 face emissivity. The emissivity (ε) of the outer wall surface was measured with
 296 an infrared camera, and a value of 0.32 was obtained. The convection coeffi-
 297 cient (h_∞) was calculated using Churchill's correlation for horizontal cylinders
 298 (Churchill and Chu, 1975).

299 [Figure 5 about here.]

300 Heat conduction in the wall was considered to be two-dimensional to take the
 301 temperature variations along the radius and the circumferential direction of the
 302 wall into account. An explicit finite difference method was used to solve the
 303 transient heat conduction equation. The energy balance method was applied by
 304 dividing the wall into nodes in the azimuthal direction ($\Delta\theta$) and radial direction
 305 (Δr). The temperature at the midpoint of cell (i, j) is called $T_{i,j}$. The geometry
 306 of the cell is a circular trapezoid of sides Δr and $r \Delta\theta$, as shown in Figure 6.

307 [Figure 6 about here.]

308 The thermal coupling between the cells is modeled by thermal conductances.
 309 The conductances in the circumferential direction between cells $(i-1, j)$ and
 310 (i, j) and cells (i, j) and $(i+1, j)$ are

$$K_{i-0.5,j} = K_{i+0.5,j} = \frac{L \Delta r k}{r_j \Delta\theta} \quad \text{for } i = 1 \dots N_k \quad (8)$$

311 The general expressions for conductance that are valid for the inner nodes along
 312 the radial direction are

$$K_{i,j-0.5} = \frac{L k \Delta \theta}{\ln \frac{r_j}{r_{j-1}}} \quad \text{for } j = 2 \dots M_k \quad (9)$$

$$K_{i,j+0.5} = \frac{L k \Delta \theta}{\ln \frac{r_{j+1}}{r_j}} \quad \text{for } j = 1 \dots M_k - 1 \quad (10)$$

313 The inner cell along the radial direction ($j = 1$) is in contact with the molten
314 salt; thus, the conductance results in

$$K_{i,0.5} = \frac{L}{\frac{1}{\Delta \theta r_i h_i} + \frac{1}{\Delta \theta k \ln \frac{r_1}{r_i}}} \quad (11)$$

315 The outer cell along the radial direction ($j = M_k$) is exposed to the atmo-
316 sphere; thus, the conductance results in

$$K_{i,M_k+0.5} = \frac{L}{\frac{1}{\Delta \theta k \ln \frac{r_o}{r_{M_k}}} + \frac{1}{\Delta \theta r_o h_{(conv+rad)_i}}} \quad (12)$$

317 Figure 6 shows a scheme of the incident/outgoing heat flows associated with
318 an internal cell. The heat flows through the left ($Q_{i-0.5,j}$) and right ($Q_{i+0.5,j}$)
319 boundaries of a cell are defined by the following expressions:

$$Q_{i-0.5,j}(t) = K_{i-0.5,j} (T_{i-1,j}(t) - T_{i,j}(t)) \quad (13)$$

$$Q_{i+0.5,j}(t) = K_{i+0.5,j} (T_{i,j}(t) - T_{i+1,j}(t)) \quad (14)$$

320 The heat flows through the inner ($Q_{i,j-0.5}$) and outer ($Q_{i,j+0.5}$) radius bound-
321 aries are expressed as follows:

$$Q_{i,j-0.5}(t) = K_{i,j-0.5} (T_{i,j-1}(t) - T_{i,j}(t)) \quad (15)$$

$$Q_{i,j+0.5}(t) = K_{i,j+0.5} (T_{i,j}(t) - T_{i,j+1}(t)) \quad (16)$$

322 The energy conservation of the wall is solved to obtain the temperature field of
323 the wall

$$\rho c_p V \frac{\partial T(r, \theta, t)}{\partial t} = Q_{i-0.5,j}(t) - Q_{i+0.5,j}(t) + Q_{i,j-0.5}(t) - Q_{i,j+0.5}(t) \quad (17)$$

324 The outer cell along the radial direction ($j = M_k$) is exposed to the induction
 325 heat flux; thus, the energy conservation of the wall results in

$$\rho c_p V \frac{\partial T(r, \theta, t)}{\partial t} = Q_{i-0.5, j}(t) - Q_{i+0.5, j}(t) + Q_{i, M_k-0.5}(t) - Q_{i, M_k+0.5}(t) + \Delta\theta r_o L q_{ind}(\theta, t) \quad (18)$$

326 where $V = \Delta\theta r_j \Delta r L$ is the cell volume. $L = 1$ in Equations (8)-(12) and Equations (17)-(18) because when solving a two-dimensional heat transfer problem,
 327 a unit depth cell is assumed.
 328

329 [Table 1 about here.]

330 3.1.2. Deflection of the pipe

331 The pipe wall is exposed to tension and compression in its different parts due
 332 to the nonuniform temperature distribution along the circumferential direction,
 333 which results in a moment that causes bending of the pipe. The tube is 4.33 m
 334 long between supports (L_T), and the center of the induction coil, which provides
 335 the heat flux, is positioned at 2.63 m from the first support, as shown in Figure
 336 7. Deflection $\delta(z, t)$ and rotation $\Theta(z, t)$ are considered to be zero at the ends,
 337 but the tube can elongate freely.

$$\delta(z, t) = 0 \quad \text{for } z = 0, L_T \quad (19)$$

$$\Theta(z, t) = 0 \quad \text{for } z = 0, L_T \quad (20)$$

338 [Figure 7 about here.]

339 The moment induced by the circumferential temperature gradient $M_T(t)$ is
 340 expressed as

$$M_T(t) = 2 E \alpha \int_0^\pi \int_{r_i}^{r_o} T(r, \theta, t) r^2 \cos \theta dr d\theta \quad (21)$$

341 where E is the Modulus of Elasticity, and α is the thermal expansion coefficient.
 342 The relation between the deflection and the moment $M(z, t)$ is expressed as
 343 (Gere, 2004)

$$\frac{d^2(\delta(z, t))}{dz^2} = \frac{M(z, t)}{E I} \quad (22)$$

344 where I is the moment of inertia of a circular pipe $\frac{\pi}{4}(r_o^4 - r_i^4)$. To obtain the
 345 deflection and bending moment from Equation (22), the reactions and moments
 346 at the supports of the pipe are obtained

$$R_a + R_b = 0 \quad (23)$$

$$M_a - R_a \cdot L_T - M_b = 0 \quad (24)$$

347 The bending moment along the length of the pipe between supports is ob-
 348 tained taking the moment equilibrium at point x

$$M(z, t) = -M_a + R_a \cdot z \quad \text{for } 0 \leq z < L_1 \quad (25)$$

$$M(z, t) = -M_a + R_a \cdot z + M_T(t) \quad \text{for } L_1 \leq z < L_2 \quad (26)$$

$$M(z, t) = -M_a + R_a \cdot z \quad \text{for } L_2 \leq z \leq L_T \quad (27)$$

349 where L_1 and L_2 are the lengths from the first support to the beginning and end
 350 of the induction coil, respectively. Substituting Equations (25)-(27) into Equa-
 351 tion (22) and integrating and imposing the boundary conditions, the deflection
 352 of the pipe can be expressed as

$$\delta(z, t) = \frac{M_T(t)}{EI} \left(\frac{(L_1 - L_2)(L_1 + L_2 - L_T)}{L_T^3} z^3 - \frac{(L_1 - L_2)(3L_1 + 3L_2 - 4L_T)}{2L_T^2} z^2 \right)$$

for $0 \leq z < L_1$

(28)

353

$$\delta(z, t) = \frac{M_T(t)}{EI} \left(\frac{(L_1 - L_2)(L_1 + L_2 - L_T)}{L_T^3} z^3 + \left(1 - \frac{(L_1 - L_2)(3L_1 + 3L_2 - 4L_T)}{L_T^2} \right) \frac{z^2}{2} - \right.$$

$L_1 z + \frac{L_1^2}{2}$) for $L_1 \leq z < L_2$

(29)

$$\delta(z, t) = \frac{M_T(t)}{EI} \left(\frac{(L_1 - L_2)(L_1 + L_2 - L_T)}{L_T^3} z^3 - \frac{(L_1 - L_2)(3L_1 + 3L_2 - 4L_T)}{2L_T^2} z^2 + \right.$$

$(L_2 - L_1)z + \frac{L_1^2 - L_2^2}{2}$) for $L_2 \leq z \leq L_T$

(30)

354 *3.2. Inverse problem*

355 In this work, an inverse algorithm is proposed to obtain the unknown time-
 356 and space-dependent heat flux received by the pipe from the knowledge of tem-
 357 perature measurements of the external wall of the pipe. For solving the inverse
 358 heat conduction problem, the conjugate gradient method with adjoint problem
 359 for parameter estimation was used (Özisik and Orlande, 2000). The formula-
 360 tion consists of the direct problem, which was explained in the previous section;
 361 the sensitivity problem; the adjoint problem; and the gradient equations. For
 362 solving the inverse problem, the unknown function q_{ind} was parameterized

$$q_{ind} = P \cdot C(\theta, t) \quad (31)$$

363 where P is the unknown parameter, and $C(\theta, t)$ is a trial function that was
 364 estimated by the knowledge of the area occupied by the coil and the magnetic
 365 flux concentrator ($-15^\circ \leq \theta \leq 15^\circ$), and the electrical power of the induction
 366 heater over time W_{ind}

$$C(\theta, t) = \begin{cases} W_{ind}(t) & \text{if } \theta \leq 15^\circ \\ 0 & \text{if } \theta > 15^\circ \end{cases} \quad (32)$$

367 As stated above, the aim of the inverse problem is to determine the unknown
 368 parameter P from the wall temperature measurements at $r = r_o$ and at different
 369 circumferential positions, denoted as $Y_{r=r_o, \theta=\theta_m}$. Therefore, the solution of the
 370 inverse problem is to minimize the following functional:

$$J[P] = \sum_{m=1}^{M_n} \int_{t=0}^{t_f} (T_{r=r_o, \theta=\theta_m} - Y_{r=r_o, \theta=\theta_m})^2 dt \quad (33)$$

371 where M_n is the total number of temperature sensors (see Figure 3), t_f
 372 is the total time in which the experimental measurements are acquired, and
 373 $T_{r=r_o, \theta=\theta_m}$ is the numerical solution at measurement positions obtained from
 374 the direct problem, which was previously calculated by using an estimated heat
 375 flux $q_{ind_{r=r_o}}^k$.

376 *3.2.1. Sensitivity problem*

377 The sensitivity function $\Delta T = \Delta T(r, \theta, t)$, which is the solution of the sen-
 378 sitivity problem, is defined as the directional derivative of the temperature T
 379 in the direction of the perturbation of the unknown function (Alifanov, 1994).
 380 The sensitivity problem can be formulated by assuming that when the unknown
 381 $q_{ind_{r=r_o}}$ is perturbed by $\Delta q_{ind_{r=r_o}}$, then T is perturbed by ΔT . Therefore, re-
 382 placing $q_{ind_{r=r_o}}$ by $(q_{ind_{r=r_o}} + \Delta q_{ind_{r=r_o}})$ and T by $(T + \Delta T)$ in the direct
 383 problem, and subtracting the direct problem from the resulting expressions, the
 384 heat diffusion equation for the sensitivity problem is obtained:

$$\rho c_p \frac{\partial \Delta T}{\partial t} = \frac{k}{r} \frac{\partial}{\partial r} \left(r \frac{\partial \Delta T}{\partial r} \right) + \frac{k}{r^2} \frac{\partial^2 \Delta T}{\partial \theta^2} \quad (34)$$

385 The boundary and the initial conditions of the sensitivity problem are expressed
 386 as follows:

$$k \frac{\partial \Delta T}{\partial r} = h_i \Delta T \text{ at } r = r_i \quad (35)$$

$$k \frac{\partial \Delta T}{\partial r} = -h_{conv+rad} \Delta T + \Delta q_{ind} \text{ at } r = r_o \quad (36)$$

$$\frac{\partial \Delta T}{\partial \theta} = 0 \text{ at } \theta = 0, \pi \quad (37)$$

$$\Delta T = 0 \text{ for } t = 0 \quad (38)$$

387 where Δq_{ind} is defines as follows

$$\Delta q_{ind} = \Delta P \cdot C(\theta, t) \quad (39)$$

388 The sensitivity problem was solved in the same manner as that for the direct
 389 problem.

390 *3.2.2. Adjoint problem*

391 As stated above, the objective of the inverse problem is to minimize Equation
 392 (33), considering that T has to satisfy the direct problem. A Lagrange multiplier
 393 $\lambda = \lambda(r, \theta, t)$, which is necessary to obtain the gradient of Equation (33), was
 394 obtained by solving the adjoint problem, which consists of multiplying Equation

395 (1) by λ and integrating the expression over space and time. The resulting
 396 expression is then added to Equation (33) to obtain

$$J[P] = \sum_{m=1}^{M_n} \int_{t=0}^{t_f} (T_{r=r_o, \theta=\theta_m} - Y_{r=r_o, \theta=\theta_m})^2 dt + \int_{t=0}^{t_f} \int_{r_i}^{r_o} \int_0^\pi \lambda \left(\frac{k}{r} \frac{\partial}{\partial r} \left(r \frac{\partial T}{\partial r} \right) + \frac{k}{r^2} \frac{\partial^2 T}{\partial \theta^2} - \rho c_p \frac{\partial T}{\partial t} \right) r d\theta dr dt \quad (40)$$

397 For obtaining the variation of the functional $\Delta J[P]$, $q_{ind_{r=r_o}}$ was perturbed
 398 by $\Delta q_{ind_{r=r_o}}$ and T was perturbed by ΔT , and then Equation (40) was sub-
 399 tracted from the resulting expression:

$$\Delta J[P] = \sum_{m=1}^{M_n} \int_{t=0}^{t_f} \int_0^\pi 2 (T_{r=r_o, \theta=\theta_m} - Y_{r=r_o, \theta=\theta_m}) \Delta T \delta(\theta - \theta_m) r_o d\theta dt + \int_{t=0}^{t_f} \int_{r_i}^{r_o} \int_0^\pi \lambda \left(\frac{k}{r} \frac{\partial}{\partial r} \left(r \frac{\partial \Delta T}{\partial r} \right) + \frac{k}{r^2} \frac{\partial^2 \Delta T}{\partial \theta^2} - \rho c_p \frac{\partial \Delta T}{\partial t} \right) r d\theta dr dt \quad (41)$$

400 where $\delta(\cdot)$ is the Dirac function. Integrating the term involving the second
 401 derivative in the radial direction by parts and using the boundary conditions
 402 of the sensitivity problem (Equations (35) and (36)), the following result is
 403 obtained:

$$\int_{r_i}^{r_o} k \lambda \frac{\partial}{\partial r} \left(r \frac{\partial \Delta T}{\partial r} \right) dr = r_o \lambda_{r=r_o} \Delta q_{ind_{r=r_o}} - \left(h_{conv+rad} \lambda_{r=r_o} + k \frac{\partial \lambda_{r=r_o}}{\partial r} \right) r_o \Delta T_{r=r_o} + \left(-h_i \lambda_{r=r_i} + k \frac{\partial \lambda_{r=r_i}}{\partial r} \right) r_i \Delta T_{r=r_i} + \int_{r_i}^{r_o} k \frac{\partial}{\partial r} \left(r \frac{\partial \lambda}{\partial r} \right) \Delta T dr \quad (42)$$

404 Integrating by parts the term of Equation (41) involving the second derivative in
 405 the circumferential direction and using the boundary conditions of the sensitivity
 406 problem (Equation (37)), the following expression is obtained:

$$\int_0^\pi k \frac{\lambda}{r} \frac{\partial^2 \Delta T}{\partial \theta^2} d\theta = \frac{k}{r} \frac{\partial \lambda_{\theta=0}}{\partial \theta} \Delta T_{\theta=0} - \frac{k}{r} \frac{\partial \lambda_{\theta=\pi}}{\partial \theta} \Delta T_{\theta=\pi} + \int_0^\pi \frac{k}{r} \frac{\partial^2 \lambda}{\partial \theta^2} \Delta T d\theta \quad (43)$$

407 Integrating by parts the term of Equation (41) involving the derivative in
 408 time and using the initial condition of the sensitivity problem (Equation (38)),

409 we obtain

$$\int_0^{t_f} \rho c_p \lambda r \frac{\partial \Delta T}{\partial t} dt = \rho c_p r \lambda_{t=t_f} \Delta T_{t=t_f} - \int_0^{t_f} \rho c_p r \frac{\partial \lambda}{\partial t} \Delta T dt \quad (44)$$

410 Substituting Equations (42)-(44) into Equation (41), the following expression

411 for the variation of the functional is obtained:

$$\begin{aligned} \Delta J[P] = & \int_{t=0}^{t_f} \int_{r_i}^{r_o} \int_0^\pi \left(k \frac{\partial}{\partial r} \left(r \frac{\partial \lambda}{\partial r} \right) + \frac{k}{r} \frac{\partial^2 \lambda}{\partial \theta^2} + \rho c_p r \frac{\partial \lambda}{\partial t} \right) \Delta T d\theta dr dt + \\ & \int_{t=0}^{t_f} \int_0^\pi \left(-h_i \lambda_{r=r_i} + k \frac{\partial \lambda_{r=r_i}}{\partial r} \right) r_i \Delta T_{r=r_i} d\theta dt + \\ & \int_{t=0}^{t_f} \int_0^\pi \left(-h_{conv+rad} \lambda_{r=r_o} - k \frac{\partial \lambda_{r=r_o}}{\partial r} + \sum_{m=1}^{M_n} 2(T_{r=r_o} - Y_{r=r_o}) \delta(\theta - \theta_m) \right) r_o \Delta T_{r=r_o} d\theta dt + \\ & \int_{t=0}^{t_f} \int_{r_i}^{r_o} \frac{k}{r} \frac{\partial \lambda_{\theta=0}}{\partial \theta} \Delta T_{\theta=0} dr dt - \int_{t=0}^{t_f} \int_{r_i}^{r_o} \frac{k}{r} \frac{\partial \lambda_{\theta=\pi}}{\partial \theta} \Delta T_{\theta=\pi} dr dt - \\ & \int_{r_i}^{r_o} \int_0^\pi \rho c_p r \lambda_{t=t_f} \Delta T_{t=t_f} d\theta dr + \int_{t=0}^{t_f} \int_0^\pi r_o \lambda_{r=r_o} \Delta q_{ind_{r=r_o}} d\theta dt \end{aligned} \quad (45)$$

412 The adjoint problem equations for determining λ are obtained by eliminating

413 the six first integral terms containing ΔT in Equation (45)

$$k \frac{\partial}{\partial r} \left(r \frac{\partial \lambda}{\partial r} \right) + \frac{k}{r} \frac{\partial^2 \lambda}{\partial \theta^2} + \rho c_p r \frac{\partial \lambda}{\partial t} = 0 \quad (46)$$

414

$$k \frac{\partial \lambda}{\partial r} = h_i \lambda \text{ at } r = r_i \quad (47)$$

$$k \frac{\partial \lambda}{\partial r} = -h_{conv+rad} \lambda + \sum_{m=1}^{M_n} 2(T_{r=r_o} - Y_{r=r_o}) \delta(\theta - \theta_m) \text{ at } r = r_o \quad (48)$$

$$\frac{\partial \lambda}{\partial \theta} = 0 \text{ at } \theta = 0, \pi \quad (49)$$

$$\lambda = 0 \text{ for } t = t_f \quad (50)$$

415 The adjoint problem is different from the direct problem because the condition

416 at $t = t_f$ is known rather than knowing the condition at $t = 0$, but both

417 problems can be solved in the same manner by changing the time variable as

418 $\tau = t_f - t$ for solving the adjoint problem.

419 After leading the six first integral terms of Equation (45) to vanish, the
 420 following expression for ΔJ remains:

$$\Delta J[P] = \int_{t=0}^{t_f} \int_0^\pi \lambda_{r=r_o} \Delta q_{ind_{r=r_o}} r_o d\theta dt \quad (51)$$

421 By substituting (39) into (51)

$$\Delta J[P] = \int_{t=0}^{t_f} \int_0^\pi \lambda_{r=r_o} C \Delta P r_o d\theta dt \quad (52)$$

422 The definition of the direction derivative of $J[P]$ in the direction of a vector ΔP
 423 is

$$\Delta J[P] = \nabla J[P] \Delta P \quad (53)$$

424 Comparing Equations (52) and (53), the gradient equation for the functional is
 425 obtained:

$$\nabla J[P] = J'[P] = \int_{t=0}^{t_f} \int_0^\pi \lambda_{r=r_o} C r_o d\theta dt \quad (54)$$

426 3.2.3. Conjugate gradient method

427 The iterative procedure to obtain P by minimizing the functional $J[P]$ is
 428 based on the conjugate gradient method. The unknown parameter P at the k th
 429 iteration is estimated following the expression

$$P^{k+1} = P^k - \beta^k d^k \quad (55)$$

430 where β^k is the search step size and d^k is the direction of descent

$$d^k = J'[P^k] + \gamma^k d^{k-1} \quad (56)$$

431 where γ^k is the conjugation coefficient and is calculated with the following
 432 expression:

$$\gamma^k = \frac{(J'[P^k])^2}{(J'[P^{k-1}])^2} \quad \text{with } \gamma^0 = 0 \quad (57)$$

433 The step size β^k is calculated by minimizing the functional $J[P^{k+1}]$ with
 434 respect to β^k . The functional $J[P^{k+1}]$ is expressed following Equation (33) as

$$J[P^{k+1}] = \sum_{m=1}^{M_n} \int_{t=0}^{t_f} [T_{r=r_o, \theta=\theta_m}(P^k - \beta^k d^k) - Y_{r=r_o, \theta=\theta_m}]^2 dt \quad (58)$$

435 Linearizing $T(P^k - \beta^k d^k)$ by a Taylor expansion and minimizing the resulting
 436 expression with respect to β^k , the following result is obtained:

$$\beta^k = \frac{\sum_{m=1}^{M_n} \int_{t=0}^{t_f} [(T_{r=r_o, \theta=\theta_m}(P^k) - Y_{r=r_o, \theta=\theta_m}) \Delta T(d^k)] dt}{\sum_{m=1}^{M_n} \int_{t=0}^{t_f} [\Delta T(d^k)]^2 dt} \quad (59)$$

437 where $T_{r=r_o, \theta=\theta_m}(P^k)$ is the solution of the direct problem at the measured
 438 locations $\theta = \theta_m$ by using the estimated P^k , and $\Delta T(d^k)$ is the solution of the
 439 sensitivity problem at $\theta = \theta_m$ by using $\Delta P = d^k$.

440 3.2.4. Stopping criterion

441 The stopping criterion is based on the discrepancy principle, which means
 442 that the procedure is stopped when the functional becomes lower than the vari-
 443 ance of the measurement errors:

$$J[P] < M_n \sigma^2 t_f \quad (60)$$

444 where M_n is the number of thermocouples welded to the outer surface of the
 445 wall (5 in this case), and σ is the standard deviation of the measurement errors,
 446 which is considered to be 8°C for the experiments accomplished in this work.

447 3.2.5. Iterative procedure

448 In this section, the computational algorithm to solve the inverse problem is
 449 summarized. Suppose that P^k is known at iteration k .

- 450 1. Compute q_{ind} according to Equation (31) and solve the direct problem
 451 (Equations (1)-(5)) to obtain T .
- 452 2. Check the stopping criterion (Equation (60)) and continue if it is not
 453 satisfied.
- 454 3. Solve the adjoint problem (Equations (46)-(50)) to obtain λ .
- 455 4. Calculate the gradient of the functional $J'[P]$ from Equation (54).
- 456 5. Calculate the direction of descent d^k and the conjugate coefficient γ^k from
 457 Equations (56) and (57).
- 458 6. Determine $\Delta P = d^k$, compute Δq_{ind} from Equation (39) and solve the
 459 sensitivity problem (Equations (34)-(38)) to obtain ΔT .

- 460 7. Calculate the search step size β^k (Equation (59)).
- 461 8. Calculate the new estimation P^{k+1} from Equation (55) and return to step
- 462 1.

463 3.3. Solution procedure

464 The governing equations of the inverse problem were numerically solved us-
465 ing a finite difference method, with mesh sizes of $\Delta r = 0.4$ mm and $\Delta\theta = 5^\circ$.
466 A fourth-order Runge-Kutta formulation was performed to solve the transient
467 problem. The numerical model was written in MATLAB software, and the
468 simulations were conducted with an Intel(R)Core(TM) i7-4790 3.60 GHz CPU.
469 The relative error between the measurements of the external wall temperature
470 of the tube and the numerical results obtained from the inverse problem reached
471 a maximum value of 10% when the heat flux abruptly changes at $t = 50$ s and
472 $t = 350$ s, as the induction coil starts heating and stops heating the pipe, re-
473 spectively. The relative error between calculated and measured temperature
474 when the heat flux provided by the induction heater is maximum is approxi-
475 mately 1%. Besides, the deflection of the tube caused by the unilateral heat
476 flux was calculated from the radial temperature profile obtained with the inverse
477 method, and it was compared with the measured deflection. The maximum dif-
478 ference between the measured and calculated displacements was 0.3 mm, which
479 is considered acceptable because the measurement resolution is 0.4 mm. Code
480 verification is defined as a set of methods developed to find coding mistakes
481 that affect the numerical discretization. In this case, code verification of the
482 direct problem was evaluated with the method of exact solutions (Roy, 2005;
483 ASME, 2009), which consists of contrasting the numerical solution to an exact
484 solution of the partial differential equations with specified initial and boundary
485 conditions. In particular, the wall temperature numerical solution at a time suf-
486 ficiently large for the temperature evolutions to reach steady state is compared
487 with the solution published by Holms (1952) and compiled by Logie et al. (2018)
488 to the two-dimensional steady-state conduction in a hollow cylinder subjected to
489 asymmetrical temperature distributions at the external boundary. For compar-

490 ison to the analytical solution, the boundary conditions for the numerical direct
491 problem were fixed to a known constant temperature at $r = r_i$, and known
492 variable heat flux in azimuthal direction at $r = r_o$ taken from the derivative ex-
493 pression of the temperature distribution. Negligible differences between the wall
494 temperature numerical results and the analytical solution were observed, with
495 a relative error of 0.02%. Furthermore, to verify that the transient response of
496 the wall temperature is accurately solved, the numerical solution is compared
497 to the analytical solution from Hahn and Özisik (2012) for the wall temperature
498 evolution with time of a long hollow cylinder maintained at a constant temper-
499 ature of 0 °C at inner and outer surfaces. In this case, the wall temperature is
500 only dependent on radial direction and time, and not dependent on azimuthal
501 direction. The maximum relative error between both numerical and analytical
502 temperature results is lower than 1%.

503 In this work, the sensitivity of the calculated heat flux to changes in outer sur-
504 face temperature measurements, molten salt-to-wall heat transfer coefficient,
505 and angular position of the thermocouples has been calculated. Being the stan-
506 dard deviation of the temperature measurements 8 °C, the uncertainty in the
507 calculated heat flux is 15 kW/m², which corresponds to a 2% of the obtained
508 heat flux. The standard uncertainty of molten salt-to-wall heat transfer coef-
509 ficient was considered to be 20% due to the uncertainties in the molten salt
510 thermophysical properties, the molten salt velocity measured with the flow me-
511 ter, and the experimental correlation used. The uncertainty in the heat flux
512 due to the uncertainty in the molten salt-to-wall heat transfer coefficient is 87
513 kW/m² (10% of the calculated heat flux). Finally, the uncertainty in the angu-
514 lar position of the thermocouples is 5°, caused by the slight descend of the pipe
515 due to the molten salt flow during the experiments. The uncertainty in the heat
516 flux due to the uncertainty in the angular position of the thermocouples is 120
517 kW/m², which is 15% of the obtained heat flux.

518

519 **4. Results and discussion**

520 As stated above, the main goal of this work is to obtain the unknown heat
521 flux received by the pipe from the external wall temperature measurements by
522 solving the inverse problem. Four different experiments were conducted, varying
523 the molten-salt velocity and the heating rate of the induction coil, as shown in
524 Table 1. Figure 8 shows the heat flux evolution with time using the inverse
525 method. Experiments 2, 3 and 4 were conducted following the same heating
526 sequence over time: during the first 50 seconds, the inductor is not heating
527 the tube; for the next 5 minutes, the inductor provides 4 kW_e of power for
528 heating the tube. Finally, during the last minute, the inducer switches off. In
529 the first experiment, the heating process starts at $t = 50$ s, the power linearly
530 increases up to the value of 4 kW_e over the course of 2 minutes, it remains
531 constant for 1 minute, and then it linearly decreases for 2 minutes until the
532 induction heater switches off. As shown in Figure 8, the maximum heat flux
533 generated by the induction heater (at $t=200$ s), which corresponds to 4 kW_e
534 of power, is 765 kW/m² for Experiment 1, 800 kW/m² for Experiment 2, 865
535 kW/m² for Experiment 3, and 930 kW/m² for Experiment 4. Therefore, we
536 concluded that approximately 28-34% of the electric power of the induction
537 heater is converted to thermal energy that reaches the tube, which is slightly
538 lower than the results of 40% electric-to-thermal efficiency obtained during the
539 calibration of the induction heater. Notice that, although the electric power
540 of the inductor was 4 kW_e for all the experiments, the heat flux received by
541 the pipe varied from one experiment to another, because it is affected by some
542 parameters difficult to control during the experiments, such as the distance
543 between the coil and the pipe, and the inlet and outlet temperatures of the
544 inductor cooling water.

545 [Figure 8 about here.]

546 Figure 9 shows the comparison between the external pipe temperatures ob-
547 tained using the inverse method (solid lines) and the external pipe temperature

548 measurements (markers) at different angular positions for the different experi-
549 ments. Regarding the molten-salt velocity, Figures 9 a) and b) for a velocity of
550 0.78 m/s show higher temperatures in the front side of the tube in comparison
551 with Figures 9 c) and d) for velocities of 1.21 and 2.89 m/s because the increase
552 in velocity enhances the heat transfer such that the wall temperature is reduced.
553 As shown, the temperatures obtained with the inverse method accurately fit the
554 experimental measurements. The maximum relative error for the angular po-
555 sition corresponding to $\theta = 12.5^\circ$ is approximately 10% for experiment 4 when
556 the heat flux abruptly changes at $t=50$ s and $t=350$ s, as the induction coil
557 starts heating and stops heating the pipe, respectively. The relative error be-
558 tween calculated and measured temperature when the heat flux provided by the
559 induction heater is maximum is approximately 1%.

560 [Figure 9 about here.]

561 Figure 10 shows the temperature profiles along the circumferential and ra-
562 dial positions and the heat flux profile along circumferential direction at $t = 200$
563 s. As shown, the maximum temperature corresponds to the center of the coil
564 $\theta = 0^\circ$; then, the temperature decreases, where the derivative with respect to
565 the angular position is higher from $\theta = 0^\circ$ to $\theta = 30^\circ$. Finally, the tempera-
566 ture remains nearly constant from $\theta = 60^\circ$. It is shown that lower molten-salt
567 velocities result in higher temperatures at the front side of the tube and thus a
568 greater temperature difference between the front and rear side of the tube.

569
570 Equations (31) and (32) establish that the heat flux is a step-function in
571 the circumferential direction, as it is shown in Figure 10, where the surface of
572 the pipe facing the induction coil that is reached by the heat flux spans from
573 $\theta = -15^\circ$ to $\theta = 15^\circ$.

574 [Figure 10 about here.]

575 The accuracy of the radial temperature profile can be verified by compar-
576 ing the displacement of the pipe obtained using Equations (28)-(30) with the

577 experimental measurements using the camera, as shown in Figure 11. The max-
578 imum difference between the measured and calculated displacements is 0.3 mm
579 for experiment 1 at $t=80$ s and $t=330$ s. At those moments is when the devi-
580 ation between the measured and modeled temperature difference between the
581 rear and front side is higher. Because the measurement resolution is 0.4 mm,
582 the difference between the numerical results and measurements is considered
583 acceptable. As shown in Figure 11, lower molten-salt velocities result in higher
584 displacement of the pipe because the temperature difference between the front
585 and rear sides of the tube is greater.

586 [Figure 11 about here.]

587 *4.1. Influence of the convective heat transfer coefficient between the molten salt* 588 *and the pipe wall*

589 In this section, the influence of the convective heat transfer coefficient from
590 the molten salt to the inner wall on the temperatures distribution along the
591 cross section of the pipe was studied. Differences of 20% between convective
592 heat transfer results obtained using different correlations for forced convective
593 heat transfer in straight tubes proposed by Cheesewright et al. (1992) were found
594 in the range of Reynolds and Prandtl numbers used in this work. Therefore,
595 different convective heat transfer coefficients h_i coming from the products of the
596 value from the correlation proposed by Petukhov (1970) and the scale factor
597 of 0.8 were tested. As shown in Figure 12, keeping the temperature of the
598 external wall fixed, higher convective heat transfer coefficients result in lower
599 temperatures in the internal wall. A variation of 20% in the convective heat
600 transfer results in a variation of 10% in the heat flux obtained with the inverse
601 method.

602 [Figure 12 about here.]

603 **5. Conclusions**

604 An inverse method has been used to obtain the unknown time-dependent
605 heat flux received by a pipe with a flow of molten nitrate salt at a temperature
606 of approximately 430 °C from outer surface temperature measurements. The
607 measurements were performed in a molten salt test loop at realistic operational
608 conditions of a solar tower receiver. The external surface of the pipe in the
609 measurement area was heated using an induction heater, which provided a very
610 high nonuniform heat flux that can be estimated based on the electric power
611 provided by the induction heater, but it cannot be measured with accuracy.

612
613 A set of experiments in which the molten-salt velocity and heating rate
614 were varied were conducted to obtain outer surface temperature measurements
615 along the circumferential direction for both the front and rear sides of the tube.
616 Lower molten-salt velocities resulted in higher temperatures at the front side of
617 the tube and therefore a greater temperature difference between the front and
618 rear sides of the tube because the convective heat transfer coefficient from the
619 molten salt to the wall increases with molten-salt velocity.

620
621 To solve the inverse problem, a transient numerical model of a circular pipe
622 conducting molten nitrate salt and subjected to a nonhomogeneous heat flux
623 was developed. A two-dimensional model in radial and circumferential direc-
624 tions was proposed, as thermal conduction in axial direction was shown to be
625 negligible. Once the heat flux was obtained from the outer surface temperature
626 measurements by means of the inverse method, the radial temperature profile
627 in the pipe wall was obtained. Furthermore, the deflection of the tube caused
628 by the unilateral heat flux was measured, and it was compared to the deflection
629 calculated from the radial temperature profile.

630
631 The outer surface temperature results obtained using the inverse method
632 exhibited good agreement with the experimental measurements, as the maxi-

633 mum relative error is approximately 10% for experiment 4 when the heat flux
634 abruptly changes at $t=50$ s and $t=350$ s, as the induction coil starts heating and
635 stops heating the pipe, respectively. The relative error between calculated and
636 measured temperature when the heat flux provided by the induction heater is
637 maximum is approximately 1%. The heat flux estimated using the inverse heat
638 transfer method was in the range 765-930 kW/m² in the different experiments.
639 These values are in accordance with the heat flux that the inductor provides ac-
640 cording to the calibration experiments conducted. Regarding the tube bending,
641 the maximum difference between the measured and calculated displacements of
642 the tube was 0.3 mm, which was considered acceptable as the resolution of the
643 measurement was 0.4 mm; thus, the accuracy of the radial temperature profile
644 of the pipe obtained with the inverse method was verified.

645

646 **Acknowledgments** This work was partially funded by the Ministerio de
647 Educación, Cultura y Deporte para la Formación de Profesorado Universitario
648 (FPU-04941), the Ministerio de Economía y Competitividad (Project ENE2015-
649 69486-R(MINECO,FEDER,UE) and Project ENE2016-78908-R) of the Spanish
650 Government and the Project SBPLY/17/180501/000412 of the Regional Gov-
651 ernment of Castilla-La Mancha. Assistance provided by D. Diaz, I. Pina and
652 M. Santos with the experimental installation was greatly appreciated.

653 **6. Notation**

654 c_p Specific heat [J/(kg K)]

655 C Trial function [W/m²]

656 d Direction of descent [W/m²]

657 d_i Internal diameter of the tube [m]

658 E Modulus of elasticity [GPa]

659	h_i	Convective heat transfer coefficient between the molten salt and pipe
660		wall [W/(m ² K)]
661	$h_{conv+rad}$	Mixed convective and radiative heat transfer coefficient from the outer
662		surface of the pipe to the atmosphere [W/(m ² K)]
663	h_∞	Convective heat transfer coefficient between the air and the pipe [W/(m ² K)]
664	I	Moment of inertia [m ⁴]
665	J	Inverse problem functional [K ² s]
666	k	Thermal conductivity [W/(m K)]
667	K	Conductance [W/K]
668	L	Cell length [m]
669	L_T	Total length of the tube [m]
670	N_k	Number of nodes in circumferential direction [-]
671	M	Bending moment [N m]
672	M_k	Number of nodes in radial direction [-]
673	M_T	Moment induced by circumferential temperature gradient [N m]
674	M_n	Number of measurements [-]
675	Re	Reynolds number, $Re = \frac{\rho_s u d_i}{\mu_s}$ [-]
676	P	Unknown parameter, [-]
677	Pr	Prandtl number, $Pr = \frac{\mu_s c_{p,s}}{k_s}$ [-]

678	q_{ind}	Heat flux generated by induction heater received by the tube [W/m ²]
679	Q	Heat flow [W]
680	R	Reaction force [N]
681	r	Radius [m]
682	r_i	Inner tube radius [m]
683	r_o	Outer tube radius [m]
684	t	Time [s]
685	t_f	Total duration of the experiments [s]
686	T	Wall temperature [°C]
687	T_s	Molten-salt temperature [°C]
688	T_∞	Surroundings temperature [°C]
689	u	Molten salt velocity [m/s]
690	V	Cell volume [m ³]
691	W_{ind}	Electrical power of the induction heater [W]
692	Y	Measured temperature [°C]
693	z	Axial direction [m]
694	<i>6.1. Greek symbols</i>	
695	α	Thermal expansion coefficient [K ⁻¹]

696	β	Search step size [-]
697	δ	Deflection of the tube [m]
698	γ	Conjugation coefficient [-]
699	ΔT	Sensitivity function [K]
700	Δr	Increment in radial direction [m]
701	$\Delta \theta$	Increment in circumferential direction [m]
702	ε	Emissivity [-]
703	λ	Adjoint function [-]
704	μ	Molten salt viscosity [Pa/s]
705	ρ	Density [kg/m ³]
706	σ_r	Stefan-Boltzmann constant, 5.67×10^{-8} [W/(m ² K ⁴)]
707	Θ	Rotation of the tube [-]
708	θ	Circumferential location [-]
709	τ	Transformed time coordinate [s]
710	<i>6.2. Subscripts</i>	
711	i	Node number along the circumferential direction
712	j	Node number along the radial direction
713	s	Molten salt

714 *6.3. Superscripts*

715 k Number of iteration

716 **References**

717 Alifanov, O. M., 1994. Inverse Heat Transfer Problems. Springer-Verlag.

718 ASME, 2009. V&V 20-2009: Standard for verification and validation in compu-
719 tational fluid dynamics and heat transfer.

720 Cattani, L., Maillet, D., Bozzoli, F., Rainieri, S., 2015. Estimation of the
721 local convective heat transfer coefficient in pipe flow using a 2D thermal
722 Quadrupole model and Truncated Singular Value Decomposition. Interna-
723 tional Journal of Heat and Mass Transfer 91, 1034–1045.

724 Cheesewright, R., Heeggs, P. J., Martin, B. W., Parry, W. J., Ralston, T.,
725 1992. Forced convection heat transfer in straight tubes. Tech. Rep. 92003,
726 Engineering Science Data Unit.

727 Churchill, S. W., Chu, H. H. S., 1975. Correlating equations for laminar and
728 turbulent free convection from a horizontal cylinder. International Journal of
729 Heat and Mass Transfer 18, 1049–1058.

730 Du, B.-C., He, Y.-L., Wang, K., Zhu, H.-H., 2017. Convective heat transfer
731 of molten salt in the shell-and-tube heat exchanger with segmental baffles.
732 International Journal of Heat and Mass Transfer 113, 456–465.

733 Duarte, J. P., Zhao, D., Jo, H., Corradini, M. L., 2018. Critical heat flux exper-
734 iments and a post-CHF heat transfer analysis using 2D inverse heat transfer.
735 Nuclear Engineering and Design 337, 17–26.

736 Gao, K., Qin, X., Wang, Z., Zhu, S., Gan, Z., 2016. Effect of magnetizer geom-
737 etry on the spot induction heating process. Journal of Materials Processing
738 Technology 231, 125–136.

- 739 Gere, J. M., 2004. Mechanics of materials. Thomson Learning.
- 740 Hafid, M., Lacroix, M., 2017. Inverse heat transfer prediction of the state of the
741 brick wall of a melting furnace. Applied Thermal Engineering 110, 265–274.
- 742 Hahn, D. W., Özisik, M. N., 2012. Heat conduction, 3rd Edition. John Wiley &
743 Sons, Inc.
- 744 Holms, A. G., 1952. A Biharmonic Relaxation Method for Calculating Thermal
745 Stress in Cooled Irregular Cylinders. Tech. Rep. NACA-TR-1059, Lewis Flight
746 Propulsion Lab.
- 747 Jianfeng, L., Xiangyang, S., Jing, D., Qiang, P., Yuliang, W., 2013a. Convective
748 heat transfer of high temperature molten salt in transversely grooved tube.
749 Applied Thermal Engineering 61, 157–162.
- 750 Jianfeng, L., Xingyang, S., Jing, D., Jianping, Y., 2013b. Transition and turbu-
751 lent convective heat transfer of molten salt in spirally grooved tube. Exper-
752 imental Thermal Fluid Science 47, 180–185.
- 753 Kim, H., Kim, H., Lee, S., Kim, J., 2018. A study on heat transfer characteris-
754 tics of quinary molten salt mixture. International Journal of Heat and Mass
755 Transfer 127, 465–472.
- 756 Kruienza, A. M., Kolb, W., Briggs, R. J., Chistian, J., Ray, D., Gill, D.,
757 Kelton, J., Chisman, K., 2014. Loop for the Observation of Film Temperature
758 Effects on Descomposition (LOFTED). Tech. Rep. SAND2014-18103, Sandia
759 National Laboratories.
- 760 Liu, T., Montefort, J., Standfield, S., Palluconi, S., Crafton, J., Cai, Z., 2018.
761 Analytical inverse heat transfer method for temperature-sensitive-coating
762 measurement on a finite base. International Journal of Heat and Mass Trans-
763 fer 118 118, 651–662.
- 764 Logie, W. R., Pye, J. D., Coventry, J., 2018. Thermoelastic stress in concen-
765 trating solar receiver tubes: A retrospect on stress analysis methodology, and
766 comparison of salt and sodium. Solar Energy 160, 368–379.

- 767 Lu, T., Liu, B., Jian, P., Zhang, Y., Li, H., 2010. A two-dimensional inverse
768 heat conduction problem in estimating the fluid temperature in a pipeline.
769 *Applied Thermal Engineering* 30, 1574–1579.
- 770 Maillet, D., Degiovanni, A., Pasquetti, R., 1991. Inverse heat conduction applied
771 to the measurement of heat transfer coefficient on a cylinder: comparison
772 between an analytical and a boundary element technique. *Journal of Heat*
773 *Transfer* 113, 549–557.
- 774 Marugán-Cruz, C., Flores, O., Santana, D., García-Villalba, M., 2016. Heat
775 transfer and thermal stresses in a circular tube with non-uniform heat flux.
776 *International Journal of Heat and Mass Transfer* 96, 256–266.
- 777 Özisik, M. N., Orlande, H. R. B., 2000. *Inverse Heat Transfer*. Taylor and Fran-
778 cis.
- 779 Pacheco, J. E., 2002. Final Test and Evaluation Results from the Solar Two
780 Project. Tech. Rep. SAND2002-0120, Sandia National Laboratories.
- 781 Perakis, N., Haidn, O. J., 2019. Inverse heat transfer method applied to capaci-
782 tively cooled rocket thrust chambers. *International Journal of Heat and Mass*
783 *Transfer* 131, 150–166.
- 784 Petukhov, B. S., 1970. Heat transfer and friction in turbulent pipe flow with
785 variable physical properties. *Advances in Heat Transfer* 6, 503–564.
- 786 Reddy, K. S., Premjit, N. S., Somasundharam, S., 2018. In-situ prediction of
787 focal flux distribution for concentrating photovoltaic (CPV) system using in-
788 verse heat transfer technique for effective design of receiver. *Solar Energy* 159,
789 510–518.
- 790 Roy, C. J., 2005. Review of code and solution verification procedures for com-
791 putational simulation. *Journal of Computational Physics* 205, 131–156.
- 792 Smith, D. C., Chavez, J. M., 1992. A Final Report on the Phase I Testing of
793 a Molten-Salt Cavity Receiver. Tech. Rep. SAND87-2290, Sandia National
794 Laboratories.

- 795 Su, J., Silva-Neto, A. J., 2001. Two-dimensional inverse heat conduction prob-
796 lem of source strength estimation in cylindrical rods. *Applied Mathematical*
797 *Modelling* 25, 861–872.
- 798 Taler, J., Duda, P., 2006. *Solving Direct and Inverse Heat Conduction Problems*.
799 Springer.
- 800 Taler, J., Duda, P., Wegłowski, B., Zima, W., Gradziel, S., Sobota, T., Taler,
801 D., 2009. Identification of local heat flux to membrane water-walls in steam
802 boilers. *Fuel* 88, 305–311.
- 803 Taler, J., Taler, D., Ludowski, P., 2014. Measurements of local heat flux to
804 membrane water walls of combustion chambers. *Fuel* 115, 70–83.
- 805 Xiangyang, S., Jianfeng, L., Jing, D., Jianping, Y., 2014. Convective heat trans-
806 fer of molten salt in circular tube with nonuniform heat flux. *Experimental*
807 *Thermal and Fluid Science* 55, 6–11.
- 808 Yadav, M. K., Singh, S. K., Parwez, A., Khandekar, S., 2018. Inverse mod-
809 els for transient wall heat flux estimation based on single and multi-point
810 temperature measurements. *International Journal of Thermal Sciences* 124,
811 307–317.
- 812 Yang, C., Chen, W. L., Chou, H. M., Salazar, J. L. L., 2013. Inverse hyperbolic
813 thermoelastic analysis of a functionally graded hollow circular cylinder in
814 estimating surface heat flux and thermal stresses. *International Journal of*
815 *Heat and Mass Transfer* 60, 125–133.
- 816 Yang, X., Yang, X., Ding, J., Shao, Y., Fan, H., 2012. Numerical simulation
817 study on the heat transfer characteristics of the tube receiver of the solar
818 thermal power tower. *Applied Energy* 90, 142–147.
- 819 Yu-ting, W., Bin, L., Chong-fang, M., Hang, G., 2009. Convective heat transfer
820 in the laminar-turbulent transition region with molten salt in a circular tube.
821 *Experimental Thermal and Fluid Science* 33, 1128–1132.

- 822 Zavoico, A. B., 2001. Solar Power Tower Design Basis Document. Tech. Rep.
823 SAND87-2290, Sandia National Laboratories.
- 824 Zhu, Z., Qin, X., Gao, K., Chen, X., 2018. Design and research on the spot
825 inductor for obtaining local high temperature rapidly. International Commu-
826 nications in Heat and Mass Transfer 96, 122–129.

827 **List of Figures**

828	1	Photograph of the molten salt test loop.	38
829	2	Detail of the induction coil. Dimensions are in mm.	39
830	3	Details of the test section, including the positions of the induction	
831		coil and thermocouples. $\theta_1 = 12.5^\circ$, $\theta_2 = 47.5^\circ$, $\theta_3 = 72.5^\circ$,	
832		$\theta_4 = 107.5^\circ$, and $\theta_5 = 132.5^\circ$ Dimensions are in mm.	40
833	4	Thermal images for nonuniform tube temperature and uniform	
834		tube temperature. Temperatures are in $^\circ\text{C}$	41
835	5	Geometry and coordinate system.	42
836	6	Mesh in cylindrical coordinates. Definitions of heat flows (Q) to	
837		and from cell (i,j)	43
838	7	Scheme of the receiver tube (black), induction coil (yellow) and	
839		supports along the z axis. Distances are in m.	44
840	8	External pipe heat flux evolution with time at $-15^\circ \leq \theta \leq 15^\circ$,	
841		obtained using the inverse method.	45
842	9	Evolution of the external pipe temperatures at different angular	
843		positions. Markers correspond to experimental measurements,	
844		and solid lines correspond to the results obtained using the inverse	
845		method. Measured temperature shown each 10 seconds.	46
846	10	Temperature profiles along the circumferential and radial posi-	
847		tions at t=200 s from the beginning of the experiment. Purple	
848		dashed line shows the heat flux profile along the circumferential	
849		positions at t=200 s.	47
850	11	Comparison between pipe displacement obtained using the in-	
851		verse method and pipe displacement measurements using the in-	
852		frared camera. Measured displacement shown each 20 seconds.	48
853	12	Temperature profiles along the circumferential and radial posi-	
854		tions for Experiment 1 for different values of h_i coming from the	
855		products of the value from the correlation proposed by Petukhov	
856		(1970) and different scale factors: $0.8 \times h_w$ (solid line) and $1 \times$	
857		h_w (dashed line).	49



Figure 1: Photograph of the molten salt test loop.

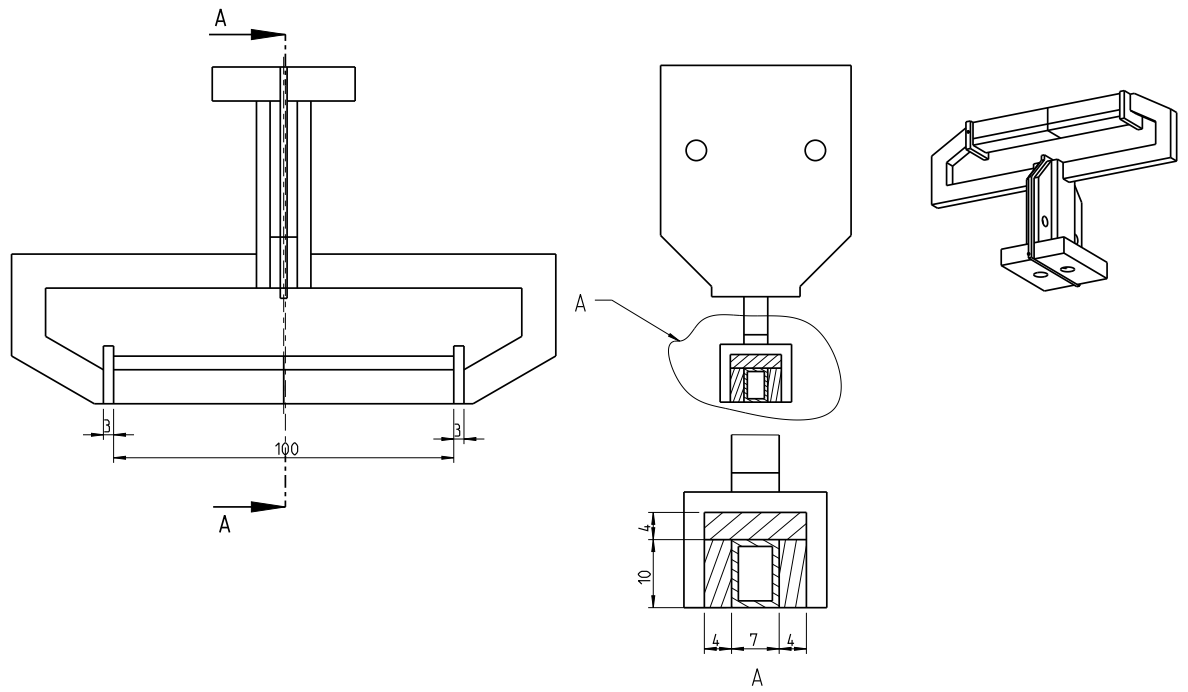


Figure 2: Detail of the induction coil. Dimensions are in mm.

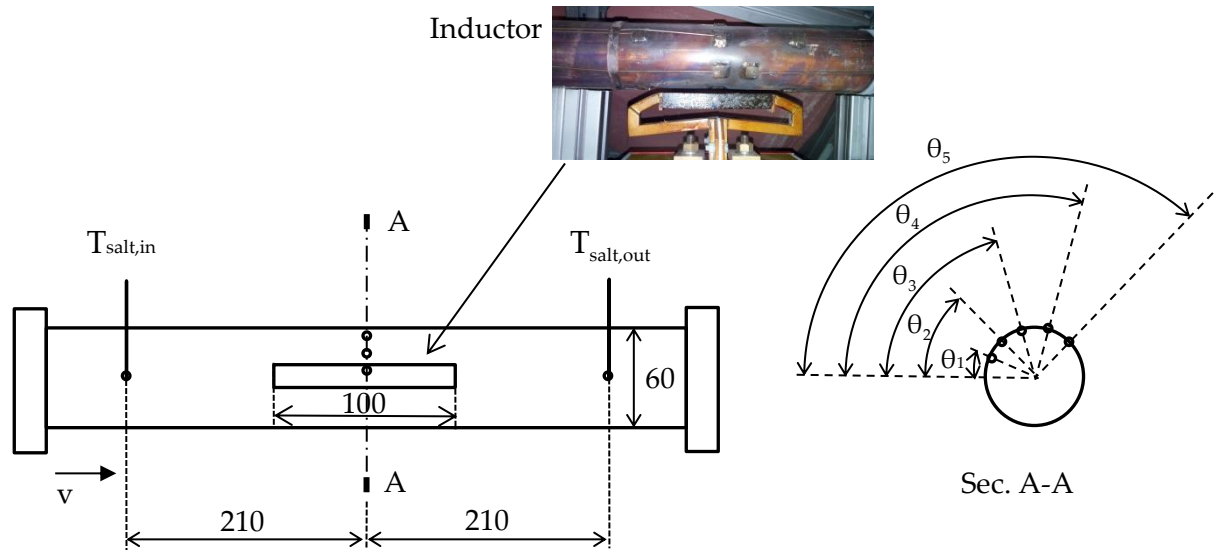


Figure 3: Details of the test section, including the positions of the induction coil and thermocouples. $\theta_1 = 12.5^\circ$, $\theta_2 = 47.5^\circ$, $\theta_3 = 72.5^\circ$, $\theta_4 = 107.5^\circ$, and $\theta_5 = 132.5^\circ$. Dimensions are in mm.

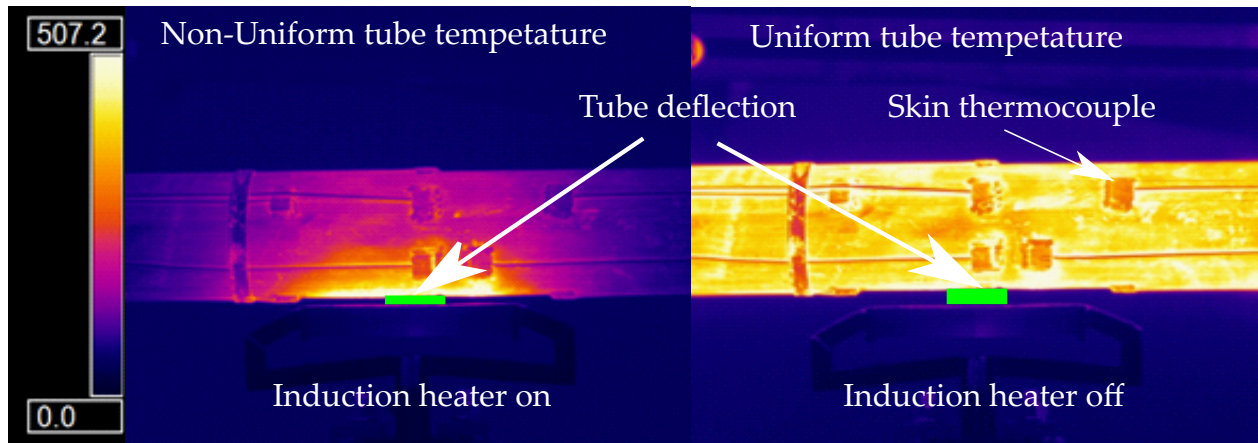


Figure 4: Thermal images for nonuniform tube temperature and uniform tube temperature. Temperatures are in °C.

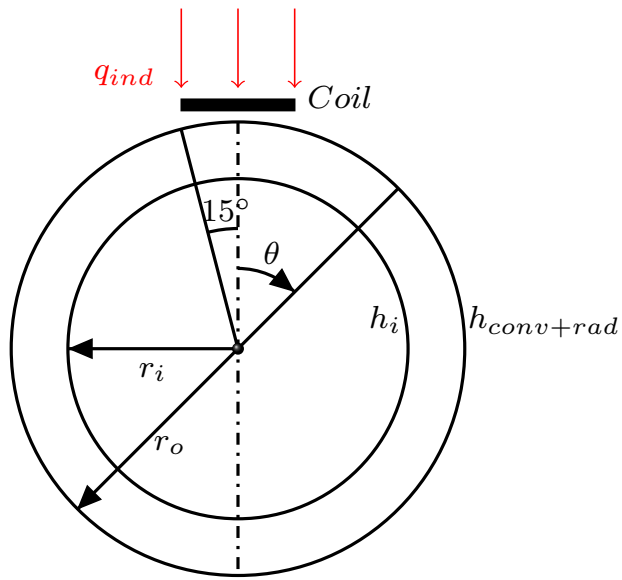


Figure 5: Geometry and coordinate system.

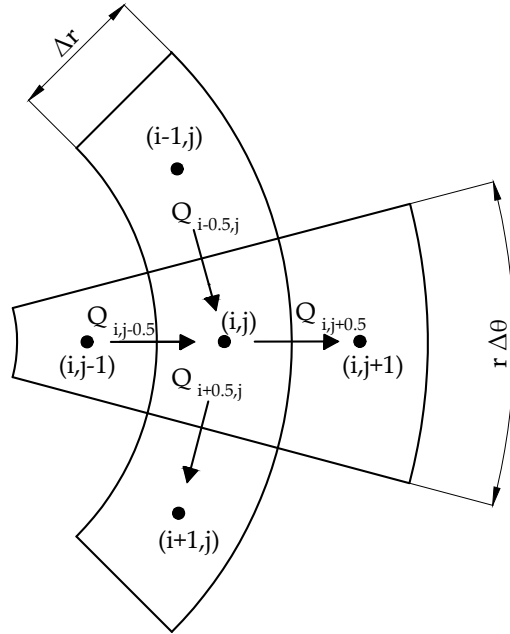


Figure 6: Mesh in cylindrical coordinates. Definitions of heat flows (Q) to and from cell (i,j)

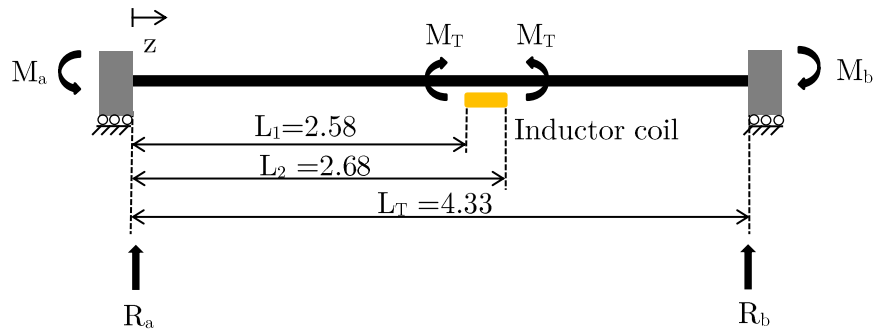


Figure 7: Scheme of the receiver tube (black), induction coil (yellow) and supports along the z axis. Distances are in m.

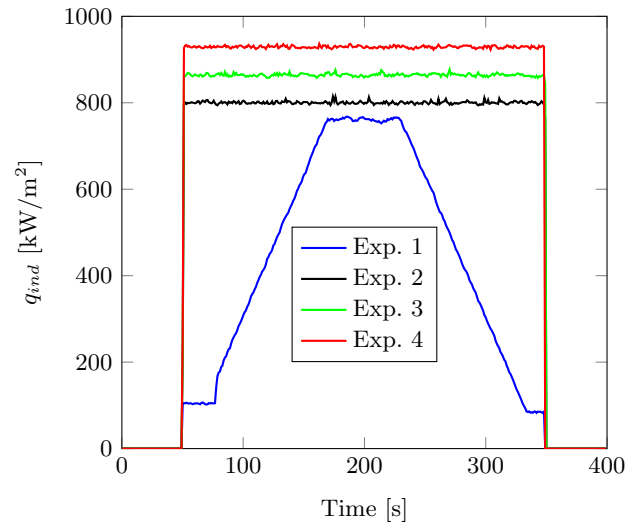
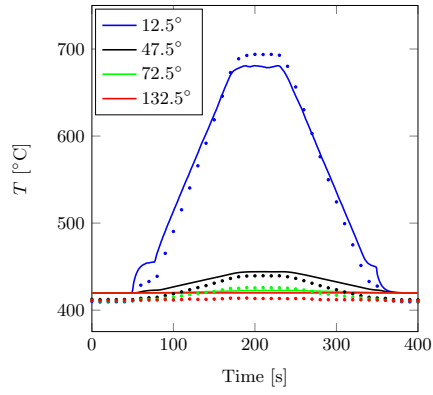
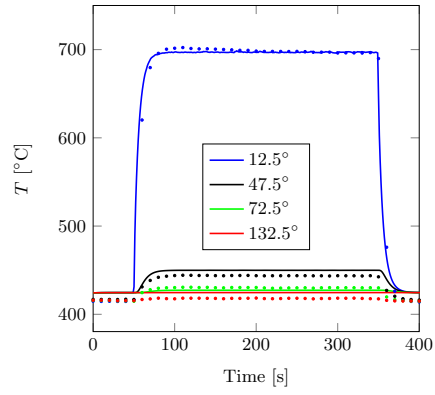


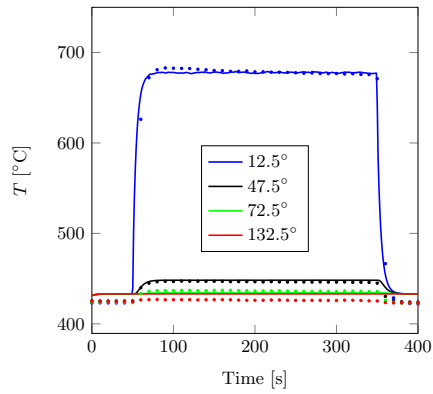
Figure 8: External pipe heat flux evolution with time at $-15^\circ \leq \theta \leq 15^\circ$, obtained using the inverse method.



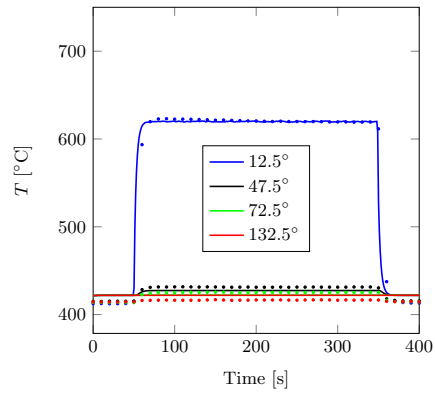
(a) Experiment 1.



(b) Experiment 2.



(c) Experiment 3.



(d) Experiment 4.

Figure 9: Evolution of the external pipe temperatures at different angular positions. Markers correspond to experimental measurements, and solid lines correspond to the results obtained using the inverse method. Measured temperature shown each 10 seconds.

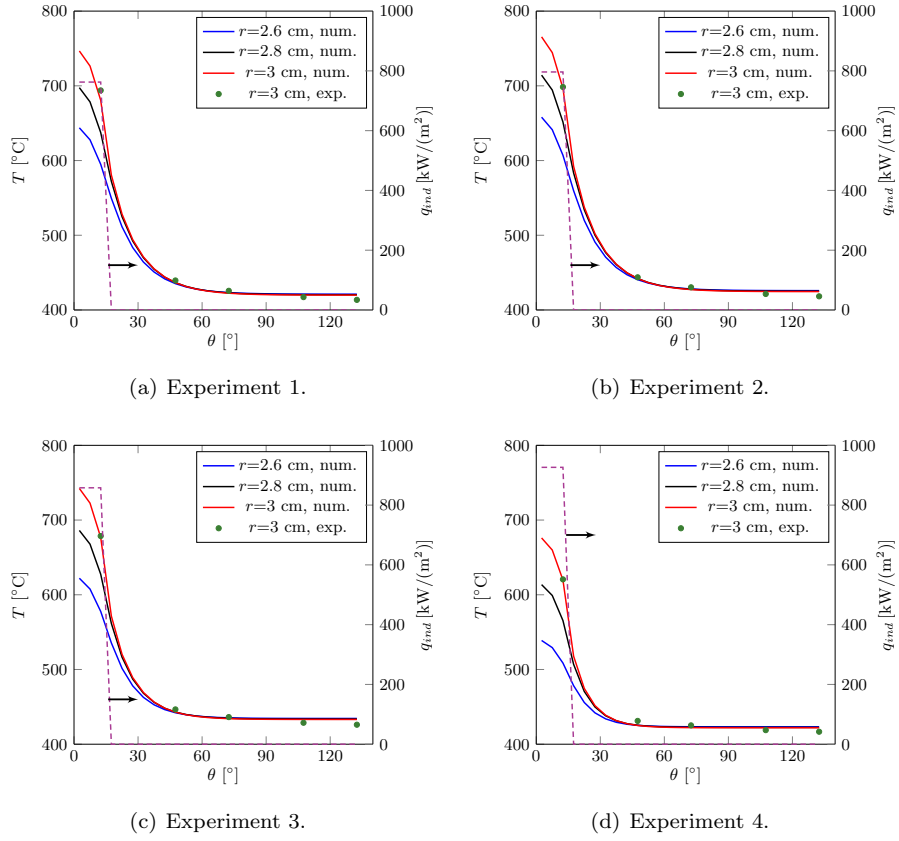
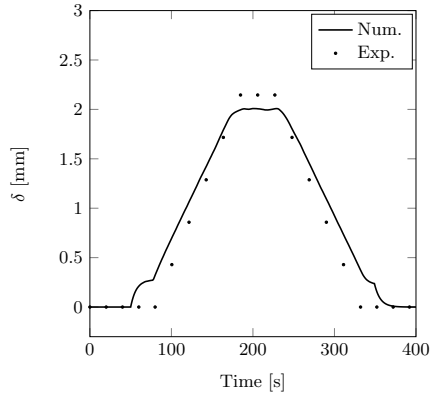
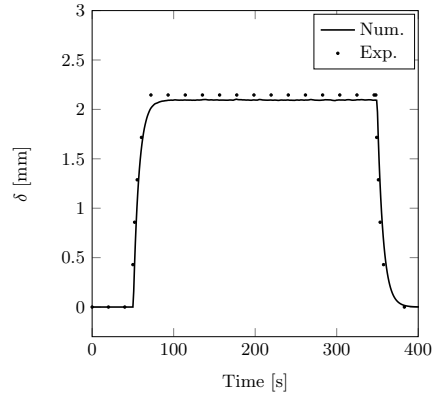


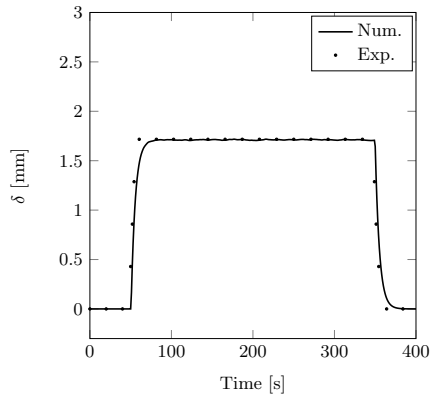
Figure 10: Temperature profiles along the circumferential and radial positions at $t=200$ s from the beginning of the experiment. Purple dashed line shows the heat flux profile along the circumferential positions at $t=200$ s.



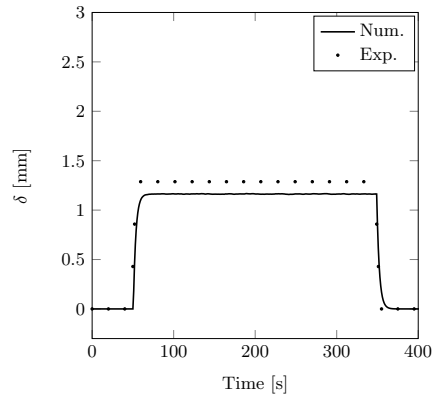
(a) Experiment 1.



(b) Experiment 2.



(c) Experiment 3.



(d) Experiment 4.

Figure 11: Comparison between pipe displacement obtained using the inverse method and pipe displacement measurements using the infrared camera. Measured displacement shown each 20 seconds.

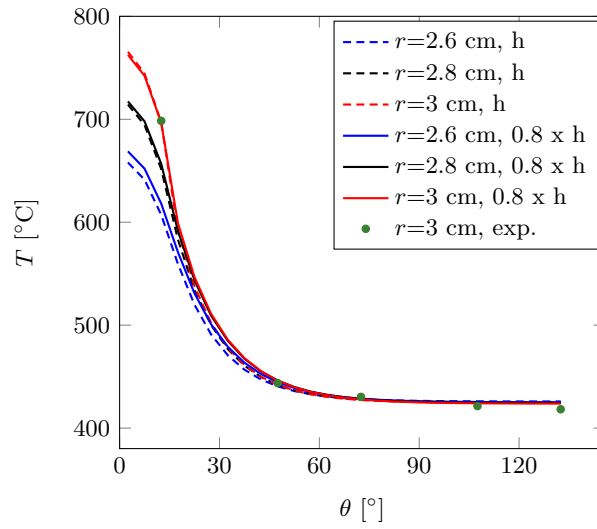


Figure 12: Temperature profiles along the circumferential and radial positions for Experiment 1 for different values of h_i coming from the products of the value from the correlation proposed by Petukhov (1970) and different scale factors: $0.8 \times h_w$ (solid line) and $1 \times h_w$ (dashed line).

858 **List of Tables**

859 1 Experimental conditions. 51

	Exp. 1	Exp. 2	Exp. 3	Exp. 4
Heating function	Ramp	Step	Step	Step
Molten-salt inlet velocity, u (m/s)	0.78	0.78	1.22	2.89
$Re = \frac{\rho_s u d_i}{\mu_s}$ (-)	46897	46977	75002	170985
$Pr = \frac{\mu_s \dot{c}_{p,s}}{k_s}$ (-)	4.64	4.55	4.44	4.63
Molten-salt inlet temperature, T_s ($^{\circ}\text{C}$)	424.5	429.1	436.1	424.7
Ambient temperature, T_{∞} ($^{\circ}\text{C}$)	34.0	32.9	31.4	34.1

Table 1: Experimental conditions.